Article

Lineage-specific canonical and non-canonical activity of EZH2 in advanced prostate cancer subtypes

Varadha Balaji Venkadakrishnan [1,2,3], Adam G. Presser[1], Richa Singh[4], Matthew A. Booker[5], Nicole A. Traphagen[1], Kenny Weng [1,6], Nathaniel C. E. Voss[1,7], Navin R. Mahadevan[1,8], Kei Mizuno[1], Loredana Puca[9], Osasenaga Idahor[1,12], Sheng-Yu Ku [1,2,3], Martin K. Bakht [1,2,3], Ashir A. Borah [3,13,14], Zachary T. Herbert[10], Michael Y. Tolstorukov [5], David A. Barbie[1], David S. Rickman [4], Myles Brown [1,11] & Himisha Beltran [1,2,3] ✉

Enhancer of zeste homolog 2 (EZH2) is a histone methyltransferase and emerging therapeutic target that is overexpressed in most castration-resistant prostate cancers and implicated as a driver of disease progression and resistance to hormonal therapies. Here we define the lineage-specific action and differential activity of EZH2 in both prostate adenocarcinoma and neuroendocrine prostate cancer (NEPC) subtypes of advanced prostate cancer to better understand the role of EZH2 in modulating differentiation, lineage plasticity, and to identify mediators of response and resistance to EZH2 inhibitor therapy. Mechanistically, EZH2 modulates bivalent genes that results in upregulation of NEPC-associated transcriptional drivers (e.g., *ASCL1*) and neuronal gene programs in NEPC, and leads to forward differentiation after targeting EZH2 in NEPC. Subtype-specific downstream effects of EZH2 inhibition on cell cycle genes support the potential rationale for co-targeting cyclin/CDK to overcome resistance to EZH2 inhibition.

Lineage plasticity is a mechanism of treatment resistance seen across many cancer types[1]. In prostate cancer, lineage plasticity is associated with resistance to hormonal therapies which can manifest clinically as a histologic transformation from prostate adenocarcinoma (PRAD) to neuroendocrine prostate cancer (NEPC)[2]. Lineage plasticity occurs in up to 15-20% of late-stage prostate cancers and is associated with poor prognosis[3,4]. Expression of androgen receptor (AR), the main driver of PRAD, is often lost in NEPC along with other luminal prostate features[5].

Epigenetic dysregulation is a major driver of cancer lineage plasticity[6,7]. We reported that NEPC arises clonally from PRAD with shared genomic features[8], acquiring distinct changes in DNA methylation and chromatin accessibility that are associated with dysregulation of lineage-determining transcription factors that distinguish NEPC from PRAD[8-11]. Epigenetic de-repression of cell fate commitment transcription factors likely facilitates lineage plasticity and NEPC progression[12]. The polycomb repressive complex (PRC2) regulates the epigenetic mark

[1]Department of Medical Oncology, Dana-Farber Cancer Institute, Boston, MA, USA. [2]Harvard Medical School, Boston, MA, USA. [3]The Broad Institute of MIT and Harvard, Cambridge, MA, USA. [4]Department of Pathology and Laboratory Medicine, Weill Cornell Medicine, New York, NY, USA. [5]Department of Informatics and Analytics, Dana-Farber Cancer Institute, Boston, MA, USA. [6]Boston College, Chestnut Hill, MA, USA. [7]Belmont Hill School, Belmont, MA, USA. [8]Department of Pathology, Brigham and Women's Hospital, Boston, MA, USA. [9]Department of Medicine, Weill Cornell Medicine, New York, NY, USA. [10]Molecular Biology Core Facilities, Dana-Farber Cancer Institute, Boston, MA, USA. [11]Center for Functional Cancer Epigenetics, Dana-Farber Cancer Institute, Boston, MA, USA. [12]Present address: Harvard University, Cambridge, MA, USA. [13]Present address: Department of Urology, University of California at San Francisco, San Francisco, CA, USA. [14]Present address: Arc Institute, Palo Alto, CA, USA. ✉e-mail: himisha_beltran@dfci.harvard.edu

H3K27me3 associated with transcriptional repression[13], and this function is mediated by its histone methyltransferase component EZH2. EZH2 is overexpressed in most castration-resistant prostate cancers including in NEPC and has emerged as a therapeutic target[8,14].

The PRC2 complex plays an important role during cell fate transitions and differentiation during normal development[15]. In this context, PRC2 acts to silence lineage-specific transcription factors[16], and loss of PRC2 in mouse models specifically induces bivalent promoters bearing both active H3K4me3 and repressive H3K27me3 acquired upon attaining a differentiated state[17,18]. In addition to its PRC2-related canonical function associated with cell identity, there is also a PRC2-independent, transcriptional co-activator function of EZH2[19]. In prostate adenocarcinoma, this non-canonical function of EZH2 can collaborate with the AR transcriptional machinery to drive AR-signaling[19–21]. The efficacy of EZH2 inhibition in PRAD preclinical models is attributable in part to the blockade of non-canonical EZH2 target genes[19]. The molecular relevance of the EZH2 co-activator function in the absence of AR, as seen in NEPC, requires further investigation.

In this study, we seek to define the mechanism of action of EZH2 in both PRAD and NEPC to determine how the underlying lineage state can impact EZH2 function and response to EZH2 inhibition in prostate cancer. We highlight how differential PRC2-mediated canonical activity contributes to a lack of lineage reversal in NEPC upon EZH2 inhibition, and in fact leads to forward differentiation towards a more terminally differentiated NE state. We investigate the relevance of the non-canonical EZH2 function which points to cell cycle mediators of response to EZH2 inhibition and a potential opportunity to co-target the cyclin/CDK pathway to overcome resistance.

Results

NEPC preclinical models show modest response to EZH2 inhibitor therapy

To understand the efficacy of EZH2 catalytic inhibition across lineage subtypes of prostate cancer, we performed cell viability and tumor growth experiments upon treatment with tazemetostat in a diverse panel of advanced prostate cancer models. Tazemetostat was used at a concentration of $5\,\mu M$ to be consistent with previously published studies[22,23] and confirmed to be above the IC_{50} in PRAD (Supplementary Fig. 1A); 6 day exposure accommodated the dilution of H3K27me3 that occurs over cell replication upon PRC2-loss[24] (Supplementary Fig. 1B). As reported previously[19], AR-positive adenocarcinoma cell lines including LNCaP and LNCaP-abl, responded to $5\,\mu M$ tazemetostat treatment over 6 days (Fig. 1A). However, AR-negative NEPC patient-derived organoid models (WCM154, WCM155, WCM1262, WCM1078)[14] showed modest or no response to $5\,\mu M$ tazemetostat. The modest response to EZH2 inhibition was also confirmed using other EZH2 catalytic inhibitors (valemetostat[25], PF-06821497[26], and GSK126[27]) two of which are in clinical trials for prostate cancer (NCT04388852, NCT03460977) (Supplementary Fig. 1C–E). The modest response to EZH2 inhibition was validated in vivo using an NEPC patient-derived xenograft (PDX) model (WCM12) where we found that the tumor growth rate was not significantly impacted when treated with tazemetostat compared to vehicle (Fig. 1B). An independent NEPC PDX model, MSKPCa4 also showed modest response to GSK126 (EZH2i) treatment (Fig. 1B). Western blotting and immunohistochemistry confirmed on-target activity of EZH2i with a significant reduction in H3K27me3 after tazemetostat in vitro and in vivo in both PRAD and NEPC models (Fig. 1C–E). RNA-Seq also supported on-target EZH2 inhibitor effects with upregulation of gene sets related to genes bearing H3K27me3 in progenitor cells (Supplementary Fig 1F). Previous studies using PRAD-to-NEPC transitioning models (i.e. Pten/Rb1/Tp53-null mouse model and LNCaP 42D[ENZR]) had reported reversal of lineage re-programming and increased AR expression upon EZH2 inhibition[28,29]. However, in our patient-derived AR-negative NEPC models, we did not observe changes in lineage genes or expression of

AR or its target genes (eg., *NKX3-1*) after EZH2 inhibition (Supplementary Fig. 1G), and gene sets related to prostate development were not significantly enriched after EZH2i therapy (Supplementary Fig. 1H). Overall, these results suggest that EZH2 inhibition may not be as effective in NEPC compared to PRAD, and that EZH2 may have a different function in NEPC beyond reversal to a luminal lineage as reported in plasticity models.

Lineage-specific dichotomy in the canonical activity of EZH2

We hypothesized that PRC2 may have different lineage-specific targets in NEPC as compared to PRAD which may contribute to the dichotomy in responses observed in the cell viability and tumor growth studies. To characterize the downstream targets of PRC2, we evaluated the genome-wide distribution of H3K27me3 by CUT&Tag in patient samples collected from rapid autopsy (9 castration-resistant PRAD, 9 NEPC) (Fig. 2A, Supplementary Data 1). Principal component analysis (PCA) of H3K27me3 signal in genome-wide 10 kb bins from patient samples demonstrated a separation of castration-resistant PRAD and NEPC samples along one of the dimensions (PC2) and a modest overlap in the other (PC1) (Fig. 2B). This was validated using UMAP and hierarchical clustering (Supplementary Fig. 2A, B). PCA and UMAP showed similar distinction between PRAD and NEPC samples when analysis was performed using broad H3K27me3 peaks (Supplementary Fig. 2C). Next, we defined 10 kb regions of enrichment specific to either PRAD or NEPC and found 30,346 regions specific to PRAD and 46,448 regions specific to NEPC (Fig. 2C). Globally, about 30% of the differentially enriched H3K27me3 regions mapped to distal intergenic regions consistent with previous reports[30], and phenotype-specific distributions were similar between castration-resistant PRAD and NEPC (Fig. 2D). Gene ontology analysis of transcription factors bearing higher levels of H3K27me3 on promoters and gene bodies in PRAD revealed enrichment of neurogenesis and central nervous system development pathways (Fig. 2E). These also included NE lineage transcription factors such as *ASCL1, PROX1, NEUROD1, LHX2, FOXA2, POU3F2*, and *INSM1* harboring high levels of H3K27me3 throughout the genomic loci and/or upstream of transcriptional start sites in PRAD and less enriched, yet present at low levels in NEPC (Fig. 2F, C). Transcription factors with high levels of H3K27me3 in NEPC as compared to castration-resistant PRAD included those related to epithelial development based on gene ontology analysis, such as *HOXB13, REST, YAP1, GATA2* (Supplementary Fig. 2D, E). H3K27me3 at the genomic loci of luminal lineage genes such as *AR, HOXB13*, and *YAP1* was present at higher levels in NEPC compared to PRAD (Supplementary Fig. 2F), however, the difference in enrichment was not as dramatic as the NE-lineage genes represented in Fig. 2F. These data were further confirmed in LuCaP patient-derived xenograft (PDX) models through analysis of published H3K27me3 ChIP-Seq data of 5 NEPC and 5 PRAD PDX tumors[31] (Supplementary Fig. 3). We found a high correlation ($r = 0.8369$; p-value < 2.2e-16) between significantly altered 10 kb regions in PRAD and NEPC in both datasets (Fig. 2H) which was particularly notable given the difference in techniques (CUT&Tag vs ChIP-Seq). H3K27me3 CUT&RUN of two representative PRAD and NEPC models (LNCaP-abl and WCM154, respectively) recapitulated the H3K27me3 profiles observed in clinical samples at the loci of the NE and luminal lineage transcription factors (Fig. 2G, Supplementary Fig. 2G).

These results confirm that PRC2 targets are distinct in castration-resistant PRAD as compared to NEPC, with NE-lineage transcription factors bearing higher levels of H3K27me3 associated with their transcriptional repression in PRAD.

Bivalent promoters are immediate targets of EZH2 inhibition

Given the lineage specificity of PRC2 targets, we sought to isolate lineage-specific genes that are induced upon EZH2 inhibition and to understand changes in their epigenetic profiles. We investigated the
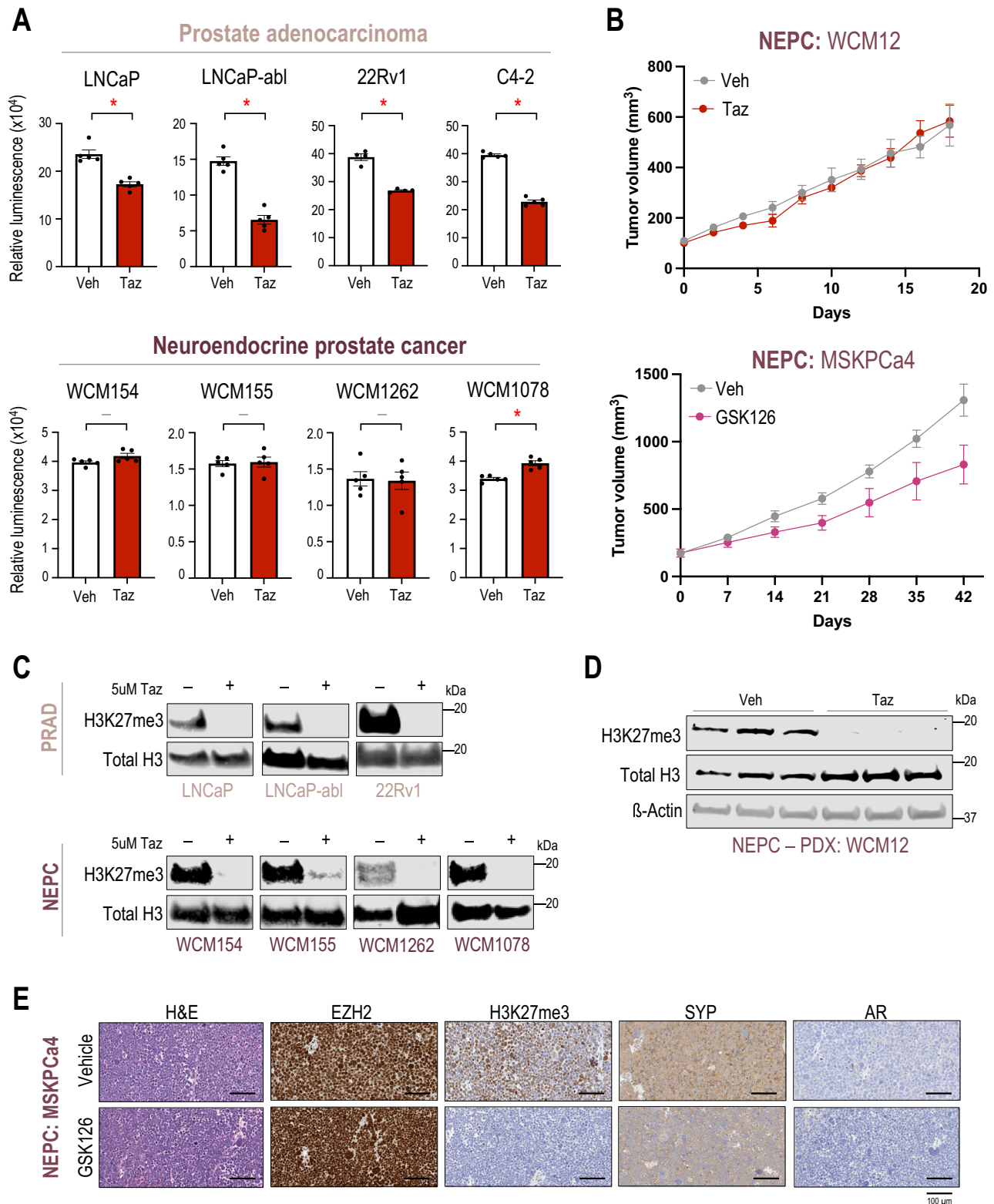
transcriptomic changes after tazemetostat treatment in LNCaP-abl (castration-resistant PRAD), which had shown the most reduction in cell viability (Fig. 1A) and in WCM154 (NEPC) which showed no response. Unsupervised k-means clustering of RNA-Seq data revealed 7 distinct clusters of genes significantly altered by tazemetostat treatment. Clusters 3 and 6 represented genes that were upregulated in WCM154 and LNCaP-abl respectively, in a model-specific manner (Fig. 3A; Supplementary Fig. 4A). We confirmed lineage-specificity of

tazemetostat-mediated induction of cluster 3 and cluster 6 genes in other PRAD and NEPC models (Supplementary Fig. 4B). As expected, tazemetostat treatment specifically lowered H3K27me3 in cluster 3 and cluster 6 genes in WCM154 and LNCaP-abl, respectively (Fig. 3B). Of note, basal expression of cluster 6 genes was higher than cluster 3 genes in LNCaP-abl and vice versa in WCM154. In LNCaP-abl, the lower expression of cluster 3 genes was associated with higher levels of H3K27me3 in LNCaP-abl (Fig. 3B). However, in WCM154, there was a

Fig. 1 | NEPC preclinical modes show modest response to EZH2i. A Prostate cancer models (Top panel – AR-driven PRAD; bottom panel – AR-indifferent NEPC) were treated with vehicle (Veh; DMSO) or 5 μM of tazemetostat (Taz). CellTiter-Glo® luminescent cell viability assay was performed after 6 days of treatment. *Columns*, means of values (*n* = 5; 22Rv1, *n* = 4); *white*, vehicle treatment; *red*, tazemetostat treatment; *bars*, SEM values; −, *p*-value > 0.05 (not significant); *, *p-value* < 0.05, all statistical analyses used Wilcoxon two-sided tests. **B** (top) WCM12, NEPC patient-derived xenograft (PDX) model was grown subcutaneously in SCID mice. Mice were randomized into treatment groups when tumor volume reached 100 mm³. Mice were treated with vehicle (*n* = 4) or 250 mg/kg b.i.d. of tazmetostat (EPZ, *n* = 5) for 18 days. Two mice in the EPZ group were euthanized before experimental endpoint adhering to animal welfare guidelines. *Connected dots*, means of values obtained from independent biological replicates; *gray*, vehicle treatment; *red*, tazemetostat treatment; *bars*, SEM values. (bottom) MSKPCa4, NPEC organoid-derived xenograft model were grown subcutaneously in

both flanks of the mice and randomized into treatment groups when tumor volume reached approximately 200 mm³. Mice were treated with vehicle (*n* = 5) or 150 mg/kg GSK126 (*n* = 5) for 6 weeks. *Connected dots*, means of values obtained from independent biological replicates; *gray*, vehicle treatment; *magenta*, GSK126 treatment; *bars*, SEM values. **C** Western blot analysis (Top panel – AR-driven PRAD; bottom panel – AR-indifferent NEPC) in a parallel experiment of (**A**) confirming the downregulation of H3K27me3 upon tazemetostat treatment in vitro. Blots were reprobed for total-histone-H3 as a loading control. Representative western blot from three independent experiments is shown. **D** Western blot analysis of tumor samples from (**B** - top) confirming the downregulation of H3K27me3 upon tazemetostat treatment in vivo. Blots were reprobed for total-histone-H3 and β-actin as loading controls. Representative western blot from two independent experiments is shown. **E** Immunohistochemistry of tumor samples from (**B** – bottom) confirming the downregulation of H3K27me3 upon GSK126 treatment in vivo. Scale bar = 100 μm.

disconnect between H3K27me3 and mRNA expression of cluster 3 genes, as they harbored higher levels of the repressive H3K27me3 mark and were also highly expressed at baseline (Fig. 3B). This led us to suspect that cluster 3 genes in WCM154 might bear bivalency at their promoters.

Bivalent promoters harbor both the transcriptional repressive H3K27me3 and activation H3K4me3 marks and have been reported as immediate targets of PRC2-loss[18]. CUT&RUN for H3K4me3 confirmed its presence at high levels in both clusters 3 and 6 in WCM154 (Fig. 3B). MHC class I genes have been reported to have conserved bivalent promoters and specifically highlighted in other small cell neuroendocrine carcinomas[32]. We also observed bivalency in MHC class I genes in NEPC and loss of H3K27me3 upon tazemetostat treatment accompanied by induction in expression (Fig. 3C, D). We validated this induction of MHC class I gene, *HLA-B* upon tazemetostat treatment in NEPC models both at the mRNA and protein level (Fig. 3D; Supplementary Fig. 4C–E). We evaluated two other genes *TMEFF2* and *SYPL2*, with prominent bivalent profiles at their promoters, and verified loss of H3K27me3 and a corresponding increase in mRNA levels upon EZH2 inhibition (Supplementary Fig. 4F–H). Of note, these genes harbored bivalency only in WCM154 (NEPC) and not in LNCaP-abl (Supplementary Fig. 4I). When characterizing the regulation of all bivalent promoters in WCM154 upon EZH2 inhibition, there was a moderate yet statistically significant inverse correlation of bivalent promoters with gene expression, as tazemetostat led to loss of H3K27me3 and gain of H3K4me3 in WCM154 (Fig. 3E). Interestingly, gene ontology analysis of tazemetostat-induced bivalent promoters with loss of H3K27me3 revealed enrichment for neurogenesis and neuron development pathways (Fig. 3F; Supplementary Fig. 4J).

To further understand how EZH2 regulates bivalent promoters in NEPC and which transcriptional machineries might be collaborating with EZH2 to induce bivalent genes upon EZH2 inhibition, we isolated regions up to 1 kb in all the bivalent promoters of WCM154 and performed HOMER motif analysis. Notably, NE-lineage transcription factor motifs such as ASCL1 and SIX4 were significantly enriched in these regions (Fig. 3G). This analysis suggests that upon inhibition of EZH2, bivalent promoters may be induced via NE-associated transcription factor (ASCL1) binding to their promoters.

As opposed to NEPC, cluster 6 genes representing immediate targets of EZH2i in PRAD (LNCaP-abl), did not harbor bivalent promoters (Supplementary Fig. 5A). The majority of genes in cluster 6 harbored low levels of H3K27me3 and high levels of H3K4me3 (Supplementary Fig. 5B). The limited number of bivalent promoters in cluster 6 in PRAD contained luminal related genes such as *NKX3-1* and *SPDEF* (Supplementary Fig. 5C). *AR* was also present in cluster 6, induced upon EZH2 inhibition, but did not harbor bivalency (Supplementary Fig. 5B). Gene ontology analyses of genes within cluster 6 were related to epithelium development and regulation of hormone levels (Supplementary Fig. 5D). Positing that there still might be

bivalent promoters that act as immediate targets of EZH2 inhibition in PRAD beyond the small numbers present within cluster 6, we isolated all genes harboring bivalent promoters in LNCaP-abl; 658 genes harbored bivalency in their promoters in LNCaP-abl, a number less than half observed in WCM154 (Fig. 3E). Of these, only 80 genes were induced upon EZH2i in LNCaP-abl, including *NKX3-1* (Supplementary Fig. 5E) and genes related to cell cycle and metabolic pathways (Supplementary Fig. 5F). Taken together, these data suggest that immediate targets of induction upon EZH2i in PRAD do not contain prominent bivalent features and are related to luminal lineage (e.g.: *AR*, *NKX3-1*, *SPDEF*). These findings are consistent with previous reports on induction of AR signaling upon EZH2 inhibition in PRAD models resulting in increased sensitivity to AR-targeted therapies[33].

Distinct PRC2 targets in PRAD and NEPC contribute to differential gene induction upon tazemetostat treatment, and bivalent promoters are preferentially induced upon EZH2 inhibition in NEPC.

Induction of NE-lineage genes upon EZH2 inhibition contributes to maintenance of a terminally differentiated state

The enrichment of pathways related to neurogenesis and neuron development upon tazemetostat treatment in NEPC may justify the lack of lineage reversal and maintenance of a terminally differentiated state that we observed in patient-derived models of NEPC. *ASCL1*, a well-established NE-lineage driver, also possessed a bivalent promoter in NEPC and was impacted by EZH2 inhibition resulting in its further upregulation (Fig. 4A, B). A number of other NE-lineage transcription factors including *PROX1, NKX2-1, OLIG1, OLIG2, ZIC1, ZIC5,* and *FOXN4* were also induced upon tazemetostat treatment in NEPC (Fig. 4C) and exhibited bivalency at their promoters (Supplementary Fig. 6A, B). EZH2 inhibition also led to an increase in the expression of NE-lineage transcription factors in other NEPC models WCM155 and WCM1262 (Supplementary Fig. 6C). Several NE-lineage adhesion or secreted proteins, including *DLL3, NPTX1, NRXN2, NTRK2,* and *NRP2*, were upregulated upon EZH2 inhibition in NEPC models and harbored bivalency at their promoters (Supplementary Fig. 6D, E)[34,35].

Using CRISPR-cas9, we established a knockout of EZH2 in WCM154 with two independent guide RNAs which subsequently led to marked reduction in H3K27me3 levels (Fig. 4D). There was an 8-fold increase in *ASCL1* mRNA levels after EZH2 knockout by qRT-PCR analysis (Fig. 4E). RNA-Seq of WCM154 with EZH2 knockout revealed multiple NE-lineage transcription factors including *NEUROD1, PROX1, LHX2, ONECUT2, NKX2-1* as significantly upregulated compared to control WCM154 (Fig. 4F), and this was accompanied by loss of bivalency (Fig. 4G). We rescued EZH2 knockout WCM154 with a recombinant dTAG-HA-EZH2 accompanied with recovery of H3K27me3 levels (Fig. 4H). RNA-Seq comparing WCM154 rescued with dTAG-HA-EZH2 versus WCM154 with EZH2 knockout verified the significant downregulation of NE-lineage transcription factors including *ASCL1, PROX1,*
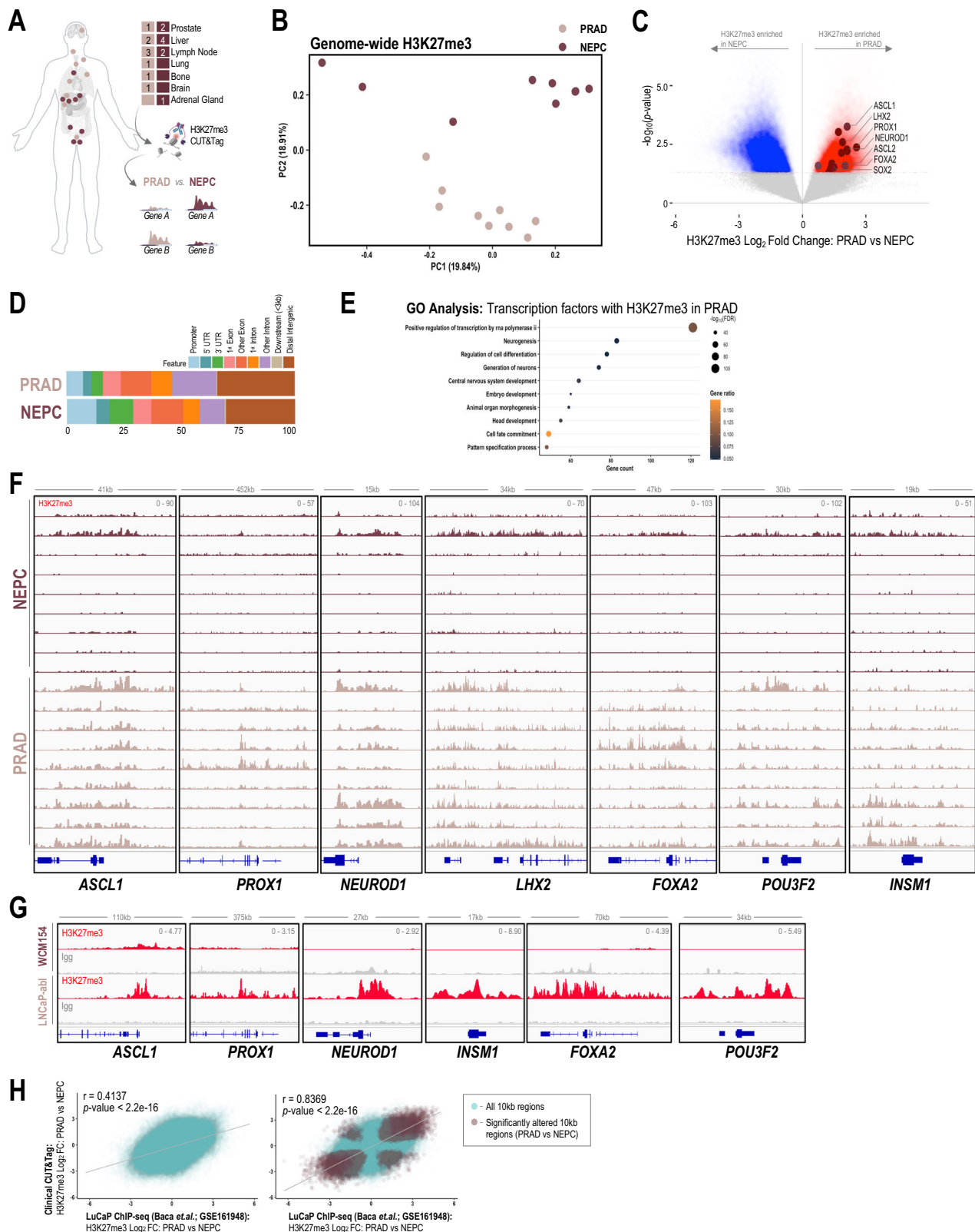
NEUROD1, and LHX2 (Fig. 4J). The dTAG system facilitates rapid targeted degradation of EZH2 within minutes after treatment with the heterobifunctional compound dTAGv1[36]. Degradation of EZH2 after 8 h did not impact its canonical substrate H3K27me3 consistent with previous reports that describe replication dilution of H3K27me3 upon PRC2 loss (Fig. 4I)[24]. We observed marked downregulation of H3K27me3 after 9 days of dTAGv1-mediated degradation of EZH2, and

RNA-seq once again confirmed the differential upregulation of NE-lineage transcription factors after 9 days of dTAGv1 treatment compared to vehicle control (Fig. 4K). ASCL1 and HES6 protein levels were markedly upregulated upon EZH2 silencing but lower when compared to EZH2 inhibition (Supplementary Fig. 6F, G). Taken together, these results demonstrate that EZH2 inhibition in terminally differentiated NEPC models leads to a further induction of NE-lineage transcription

Fig. 2 | PRC2 targets are distinct in PRAD and NEPC. A Schematic of rapid autopsy sites of NEPC and castrationresistant PRAD and workflow of H3K27me3 CUT&Tag and downstream differential analysis. Figure 2/panel A Created with BioRender.com released under a Creative Commons Attribution-NonCommercial-NoDerivs 4.0 International license. **B** H3K27me3 fragment per million (FPM) reads were calculated genome-wide for 10 kb bins for each sample. Principal component analysis of the FPM values from PRAD and NEPC samples across two dimensions; *pale pink*, castration resistant PRAD; *burgundy*, NEPC. **C** Volcano plot with differentially enriched 10 kb bins of H3K27me3 FPM values in NEPC or castration resistant PRAD samples; *blue*, H3K27me3 regions enriched in NEPC samples; *red*, H3K27me3 regions enriched in castration resistant PRAD samples; *burgundy*, NE-lineage transcription factors with enrichment of H3K27me3 at either promoter or gene body. **D** Bar plot showing distribution of subtype specific H3K27me3 enriched in castration resistant PRAD or NEPC; *light blue*, promoter; *blue*, 5' untranslated regions (UTR); *green*, 3' UTR; *pale pink*, 1st exon; *coral*, other exon; *orange*, 1st intron; *violet*, other intron; *gray*, downstream (< 3 kb); *brown*, distal intergenic. **E** Gene

ontology analysis of transcription factors with enrichment of H3K27me3 in the promoter of gene body from in castration resistant PRAD (**C**) with *p*-value < 0.05 and Log$_2$FoldChange > 0; size, -log$_{10}$FDR; *orange-black gradient*, gene ratio. **F** Screenshots from Integrative Genomics Viewer (IGV) of CUT&Tag H3K27me3 levels in castration resistant PRAD and NEPC and the genomic loci of indicated NE-lineage genes (*ASCL1, PROX1, NEUROD1, LHX2, FOXA2, POU3F2, INSM1*); *pale pink*, castration resistant PRAD samples; *burgundy*, NEPC samples. **G** Screenshots from Integrative Genomics Viewer (IGV) of CUT&RUN H3K27me3 levels in LNCaP-abl and WCM154 and the genomic loci of indicated NE-lineage genes; *gray*, IgG; *red*, H3K27me3. **H** Pearson's product-moment correlation of Log2FoldChange of H3K27me3 FPM values in PRAD (*n* = 9) compared to NEPC (*n* = 9) in Clinical CUT&Tag in this study vs LuCaP ChIP-Seq (PRAD; *n* = 5, NEPC; *n* = 5) from Baca et al.[31] (publicly available in Gene Expression Omnibus under accession code: GSE161948); *teal*, genome-wide 10 kb regions; *brown*, all significantly altered regions (PRAD vs NEPC) common in both datasets.

---

factors bearing bivalency which may be responsible for maintenance of an NE differentiated state.

Co-activator function of EZH2 may not be prominent in NEPC providing rationale for cyclin-CDK inhibition

Based on the differential canonical PRC2-associated function of EZH2 observed in PRAD as compared to NEPC, we posited that the non-canonical activity of EZH2 may also be divergent. We sought to better understand the EZH2 co-activator function and its relevance in the absence of AR signaling in NEPC by looking at genes that were downregulated with tazemetostat. After tazemetostat treatment, 93 and 54 genes were significantly downregulated in PRAD (LNCaP and LNCaP-abl, respectively), which is approximately one-third of the number of genes that were upregulated (Fig. 5A). However, in NEPC models only up to 10 genes were significantly downregulated, which suggests less of an impact of the non-canonical activity of EZH2 in NEPC (Fig. 5A). To validate this further, we employed our rescue WCM154 model with dTAG-HA-EZH2. dTAG system has been used to identify direct transcriptional targets of transcription factors after short-term degradation and transcriptomic analysis[37–39]. RNA-Seq after 8 h of degradation of EZH2 showed no differentially expressed genes in WCM154 confirming that EZH2 has limited co-activator function in NEPC (Fig. 5B). A robust gene signature containing 56 genes that represent EZH2-activated genes has been reported in PRAD and validated in hematological malignancies[20]. After tazemetostat treatment, we found that the majority of these signature genes were significantly downregulated in PRAD models but not in NEPC (Fig. 5C; Supplementary Fig. 7A). Another recent independent study by Wang et al.[21] describing the non-canonical EZH2 activating function primarily using the 22Rv1 castration-resistant PRAD model reported 130 EZH2 co-activated genes. We observed a similar pattern of these genes as downregulated in PRAD, but this was not seen in NEPC models (Supplementary Fig. 7B). We found that the non-canonical co-activator function of EZH2 in PRAD mainly impacted E2F gene signature and cell cycle regulation ([19], Supplementary Fig. 7C–E). Gene-set enrichment analysis pointed to several pathways related to cell cycle regulation with high negative enrichment in PRAD but not in NEPC (Fig. 5D). Tazemetostat-mediated downregulation of cell cycle and checkpoint genes including cyclinA and cyclinB was restricted to PRAD, with no notable regulation observed in NEPC despite high basal expression of these genes (Fig. 5E, Supplementary Fig. 7F). Western blotting of PRAD models (LNCaP and LNCaP-abl) showed downregulation of cyclins (*CCNA2, CCNB1*, and *CCNB2*) upon tazemetostat treatment validating changes seen at the mRNA level (Fig. 5F). Gene ontology analyses further confirmed that tazemetostat specifically decreased the expression of genes related to cell cycle processes (cluster2; Fig. 3A) in LNCaP-abl but not in WCM154 (Supplementary Fig. 7G). Since downregulation of cell cycle regulators upon EZH2 inhibition could

contribute to the responses seen with tazemetostat in PRAD, we hypothesized that targeting cell cycle regulators may compensate for the lack of response to EZH2 inhibition in NEPC.

CIR7-2512 is a macrocyclic cyclin-CDK2 inhibitor that blocks RxL substrate binding of the complex[40,41]. We performed IC$_{50}$ dose response analysis of CIR7-2512 for cell viability in two PRAD and two NEPC models along with an inactive enantiomer of the compound (Fig. 5G; Supplementary Fig. 8A) and found 500 nM to be an optimal dose for growth assays. CIR7-2512 treatment impeded the growth of WCM155 and WCM1262 over 6 days of treatment (Fig. 5H). Treatment with CIR7-2512 reduced cell viability of PRAD comparable to tazemetostat treatment. NEPC models that did not respond to EZH2 inhibition showed significant response to cyclin-CDK2 inhibition and combination therapy (Fig. 5I; Supplementary Fig. 8B). Effects of cell-cycle inhibition in PRAD and NEPC models were verified with an independent CDK2 inhibitor, tagtociclib (Supplementary Fig. 8C, D;[42,43]). Strong synergistic effects of combination treatment were not anticipated and were not observed[44] (Supplementary Fig. 9). Overall, the non-canonical co-activator function of EZH2 may be less prevalent in NEPC and investigating its relevance suggested a strategy for targeting or co-targeting cyclin-CDK2.

Discussion

EZH2 is an emerging therapeutic target in advanced prostate cancer yet clinical biomarkers of response have not been established. While EZH2 is known for its modulation of AR signaling in both AR-driven PRAD and in lineage plasticity models, the function of EZH2 in NEPC has not been defined[19,21,28,29,45]. Based on its important role in differentiation[13], we hypothesized that EZH2 would have variable functions in prostate cancer depending on the underlying differentiation state or phenotype (Fig. 5J).

Although EZH2 is overexpressed in nearly all NEPC tumors and has been suggested as a therapeutic target for NEPC, we observed only modest response to EZH2 inhibition in various NEPC preclinical models. EZH2 inhibition in NEPC did not result in lineage reversal back towards PRAD, but surprisingly led to a further induction of the expression of NE-lineage genes potentially pushing tumors towards a more terminally differentiated state. The full extent of forward NE-differentiation mediated by EZH2 inhibition or silencing warrants further investigation as we validated expression changes of a limited number of NE-drivers at the protein level. Epigenetic profiling coupled with genetic perturbation identified genes including NE-lineage transcription factors that acquire bivalency in their promoter preparing them to be induced as immediate targets of EZH2 inhibition. Genes such as *ASCL1, NEUROD1, ONECUT2, DLL3*, that are commonly overexpressed in NEPC, acquire H3K4me3 marks of transcriptional activation retaining low levels of H3K27me3 rendering them bivalent and poised for induction after blocking the canonical EZH2 function
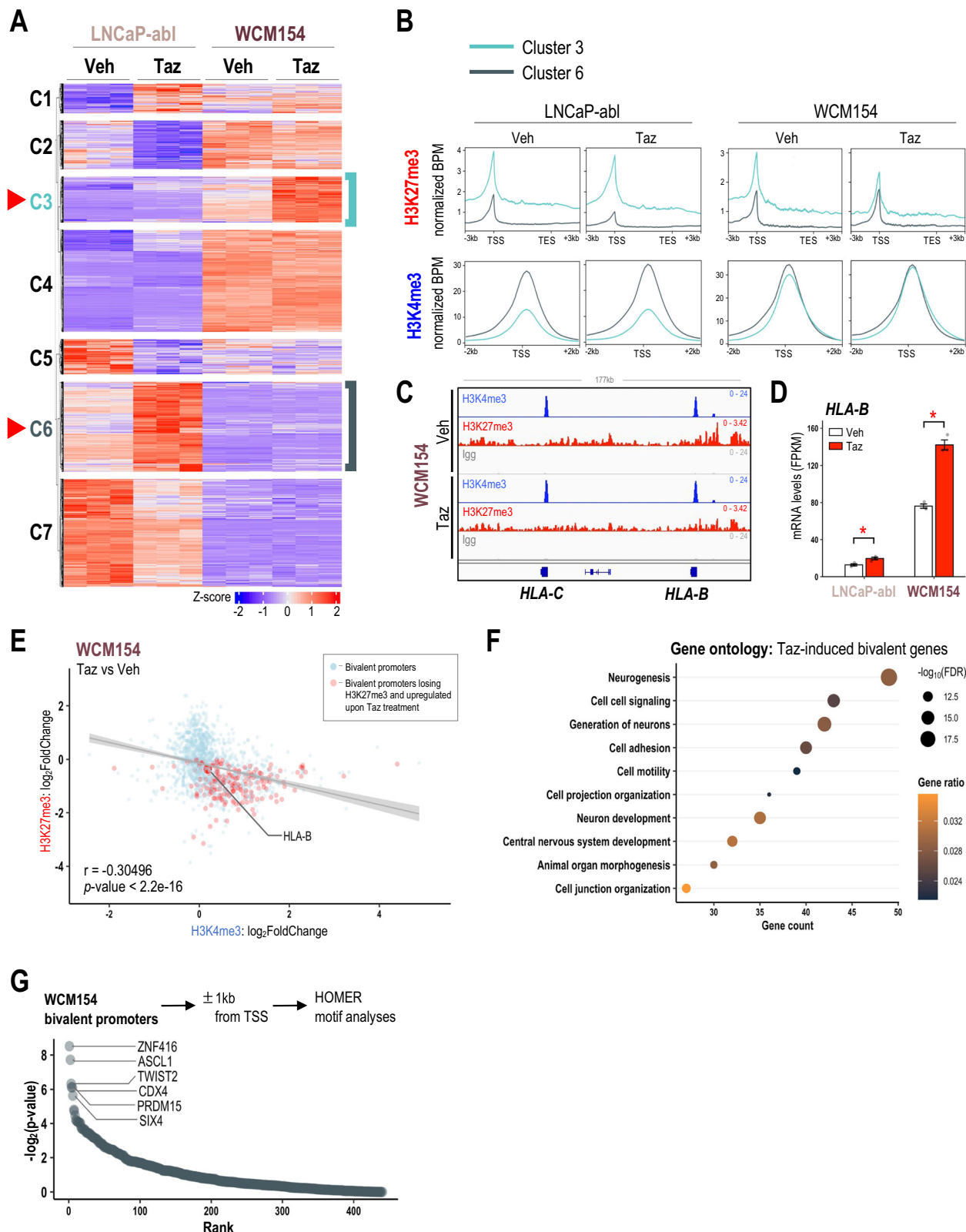
(Fig. 5J). While acquired bivalency is tissue-specific and a well-studied mechanism of cell differentiation during normal development[17,18,46], its parallel in cancer lineage plasticity and drug resistance is not well understood[47]. Whether pushing tumors to become more differentiated or neuroendocrine, and less heterogeneous, leads to new or enhanced therapeutic vulnerabilities to NEPC-directed therapies (e.g., DLL3 targeted agents) warrants further study.

MHC class I genes were also identified as bivalent genes upregulated after EZH2 inhibition in NEPC, suggesting an immunomodulatory function of PRC2 and pointing to the potential for EZH2 and immunotherapy combination strategies. There are several parallels of these findings with other cancer types. Transcriptional repression of MHC class I genes has been reported in other NE carcinomas including small cell lung cancer, merkel cell carcinoma, and neuroblastoma[48,49], and

Fig. 3 | EZH2 inhibition induces bivalent promoters in NEPC. A Clustering analysis of RNA-seq data ($n = 3$/condition/model) of PRAD or NEPC models treated with vehicle (Veh; DMSO) or 5 μM of tazemetostat (Taz) for 6 days. Unsupervised k-means clustering was performed on scaled (z-score) FPKM values of genes that were upregulated upon tazemetostat treatment in both models ($log_2FC > 0$, FDR < 0.05). Optimum number of clusters was determined using sum of squared errors (k = 7). Z-score: *red*, high; *blue*, low; *turquoise*, cluster 3 corresponding to genes tazemetostat-induced in WCM154; *teal*, cluster 6 corresponding to genes tazemetostat-induced in LNCaP-abl. **B** H3K27me3/H3K4me3 CUT&RUN from LNCaP-abl and WCM154 was analyzed and plots show profiles of normalized H3K27me3 and H3K4me3 peaks at ±3 kb of gene bodies or TSS of genes upregulated upon EZH2i treatment in LNCaP-abl (*turquoise*) or WCM154 (*teal*). **C** Screenshots from Integrative Genomics Viewer (IGV) of CUT&RUN H3K27me3 or H3K4me3 or IgG levels in LNCaP-abl and WCM154 and the genomic loci of indicated MHC class I genes with vehicle or tazemetostat treatment; *gray*, IgG; *red*, H3K27me3; *blue*, H3K4me3. **D** FPKM values of *HLA-B* from the RNA-Seq (Fig. 3A) in

vehicle or tazemetostat treated conditions in indicated models. *Columns*, means of values ($n = 3$); *white*, vehicle treatment; *red*, tazemetostat treatment; *bars*, SEM values; **p*-value < 0.05, all statistical analyses used Wilcoxon two-sided tests. **E** Scatter plot of log2FoldChange of H3K27me3 and H3K4me3 upon tazemetostat treatment as described in (**B**) on bivalent promoters in WCM154; *light blue*, bivalent promoters in vehicle condition ($n = 1535$); *red*, bivalent promoters losing H3K27me3 and corresponding genes upregulated upon tazemetostat treatment ($n = 209$; $log_2FoldChange > 0$; *p*-value < 0.05); *r* value corresponding *p*-value calculated from Pearson's product-moment correlation analysis; *gray line*, linear regression; *gray band*, standard error of regression. **F** Gene ontology of bivalent promoters losing H3K27me3 and corresponding genes upregulated upon tazemetostat treatment ($n = 209$, $log_2FoldChange > 0$; *p*-value < 0.05;) as described in (**E**); *size*, $-log_{10}$FDR; *orange-black gradient*, gene ratio. **G** HOMER analysis was performed setting the promoter region as 1 kb upstream or downstream from TSS of bivalent genes in WCM154 and significantly enriched transcription factor motifs are highlighted.

---

transcriptional repression of MHC class I genes may also be acquired as a mechanism of resistance to immunotherapy[50]. Epigenetic recovery of MHC class I expression mediated by EZH2 is associated with loss of NE differentiation in SCLC[51]. Furthermore, the MHC class I genes have been reported to be silenced in EGFR-mutant lung adenocarcinoma upon lineage transformation to small cell lung cancer[32]. Our data further supports potential combination EZH2 and immunotherapy co-strategies that are being developed clinically.

Response to EZH2 inhibition is mediated in part by its non-canonical activity[19–21]. We report cell-cycle genes as non-canonical targets of EZH2 in PRAD beyond the AR. The anti-tumor effects of EZH2 inhibition may be through downregulation of cell-cycle related genes in PRAD and other AR-low NEPC-transitioning models[28,29], potentially collaborating with its impact on AR signaling. However, this was not observed in AR-negative NEPC models and might have contributed to the limited responses to EZH2 inhibition we saw in NEPC (Supplementary Fig. 7). Using a macrocyclic inhibitor of cyclin/CDK (CIR7-2512) or the CDK2 inhibitor tagtociclib, we demonstrated in vitro activity in PRAD that was comparable to EZH2 inhibition. NEPC cells that were insensitive to EZH2 inhibition responded to either CIR7-2512 and tagtociclib. The interplay between EZH2 and other cell cycle targets (e.g., *AURKA, CHEK1, CDKN1A*) has also been reported in other contexts such as breast cancer, melanoma, non-Hodgkin's lymphoma, T-cell acute lymphoblastic leukemia[52,53]. EZH2 itself is a downstream target of RB-E2F pathway facilitating cell-cycle control[54]. Further supporting this interplay, loss of *RB1* is a mechanism of resistance to EZH2 inhibition in rhabdoid sarcoma[55]; upon *RB1* silencing, tazemetostat no longer downregulated *CCNA2*. This is also supported by a recent report that utilized a CRISPR screen in rhabdoid sarcoma and merkel cell carcinoma models and found *RB1* or *TP53* loss as a mediator of resistance to EZH2 inhibition[49,56]; these genomic alterations are also enriched in NEPC[4,8]. Furthermore, *RB1* loss by itself may contribute to the response to cyclin/CDK inhibition independent of the non-canonical function of EZH2[57].

A number of EZH2 inhibitors are being evaluated in clinical trials for castration-resistant prostate cancer, and all of these trials are biomarker-unselected (NCT04846478, NCT04179864, NCT03460977). PRC2 complex degraders (PROTACs) targeting EED and EZH2 are also under clinical development[58,59]. Identifying the patients most likely to respond will require detailed correlative analyses as well as an improved understanding of the mechanism of action of EZH2 and PRC2 in heterogeneous clinical, genomic, and phenotypic contexts. Biomarker analysis to identify AR-driven, plasticity, and NEPC sub-types, such as with cell free DNA (cfDNA) epigenetic platforms, could potentially help stratify patients and fuel the development of rational subtype-specific combination strategies[60]. Serial cfDNA analyses may also be useful to evaluate changes in differentiation state and active histone marks that occur on EZH2 therapy, with downregulation of AR

activity expected after EZH2 inhibition in castration-resistant PRAD, upregulation of AR and downregulation of NE programs in mixed/transition tumors, and upregulation of NE programs in NEPC.

Methods

Cell culture and reagents

LNCaP, C4-2, 22Rv1, and HEK293FT cells were purchased from American Type Culture Collection (ATCC) and authentication was performed using STR profiling. LNCaP, C4-2, and 22Rv1 cells were maintained in phenol red-free RPMI1640 medium (Gibco) that is supplemented with 9% fetal bovine serum (FBS) (Gibco) and 1% antibiotic-antimycotic (Gibco). LNCaP-abl[61] was a generous gift from Dr. Myles Brown's lab at Dana-Farber Cancer Institute and were maintained in phenol red-free RPMI1640 medium (Gibco) that is supplemented with 9% Charcoal-stripped fetal bovine serum (CSS) (Gibco) and 1% antibiotic-antimycotic (Gibco). HEK293FT cells were grown in phenol red containing Dulbecco's modified Eagle's medium (high glucose, Life Technologies) that is supplemented with 9% FBS and 1% antibiotic-antimycotic. All cell lines were kept in a 37 °C incubator at 5% CO_2. Cells that were used in transfection studies were seeded in medium without antibiotics. NEPC organoids, including WCM1078, WCM154, WCM155 and WCM1262 used for this study have been described previously[14]. The NEPC organoids were grown with growth-factor-reduced Matrigel (Corning). Five droplets of around 50 μl cell suspension/Matrigel mixture was pipetted onto each well of a six-well cell suspension culture plate (Greiner). The six-well plate was placed into a cell culture incubator at 37 °C and 5% CO_2 for 30 min to solidify the droplets before 2 ml prostate-specific culture medium was added to each well. The organoids were grown in prostate-specific culture medium consisting of Advanced DMEM/F12 (Invitrogen) with GlutaMAX (1×, Invitrogen), HEPES buffer (1 M, Invitrogen), 1% antibiotic-antimycotic (Gibco), B27 supplement (Gibco), N-acetylcysteine 1.25 mM (Sigma-Aldrich), mouse recombinant protein EGF 50 ng/ml (Peprotech), human recombinant FGF-10 20 ng/ml (Peprotech), recombinant human FGF-basic 1 ng/ml (Peprotech), A-83-01 500 nM (Tocris), SB202190 10 μM (Sigma-Aldrich), nicotinaminde 10 mM (Sigma-Aldrich), PGE2 1 μM (Tocris), NRG 100 μl/ml (GenScript), Y-27632-2HC1 10 μM (Selleck), Noggin conditioned medium (10%) and R-spondin conditioned medium (5%). All cell lines were tested for mycoplasma every 6 months (ABM; cat. no. G238). Tazemetostat (xcessbio; cat. no. M60122-10S), valemetostat (selleckchem; cat. no. S8926), GSK126 (xcessbio; cat. no. M60071-2S), PF-06821497 (A21388), CIR7-2512 (CirclePharma), CIR7-2724 (CirclePharma), Tagtociclib (sellckchem; cat. no. S9878) were dissolved in DMSO (sigma) for in vitro studies.

Clinical samples and H3K27me3 CUT&Tag

Tumor specimens were secured adhering to approved protocols by the DFCI and WCM Institutional Review Boards (nos. 19-883 and
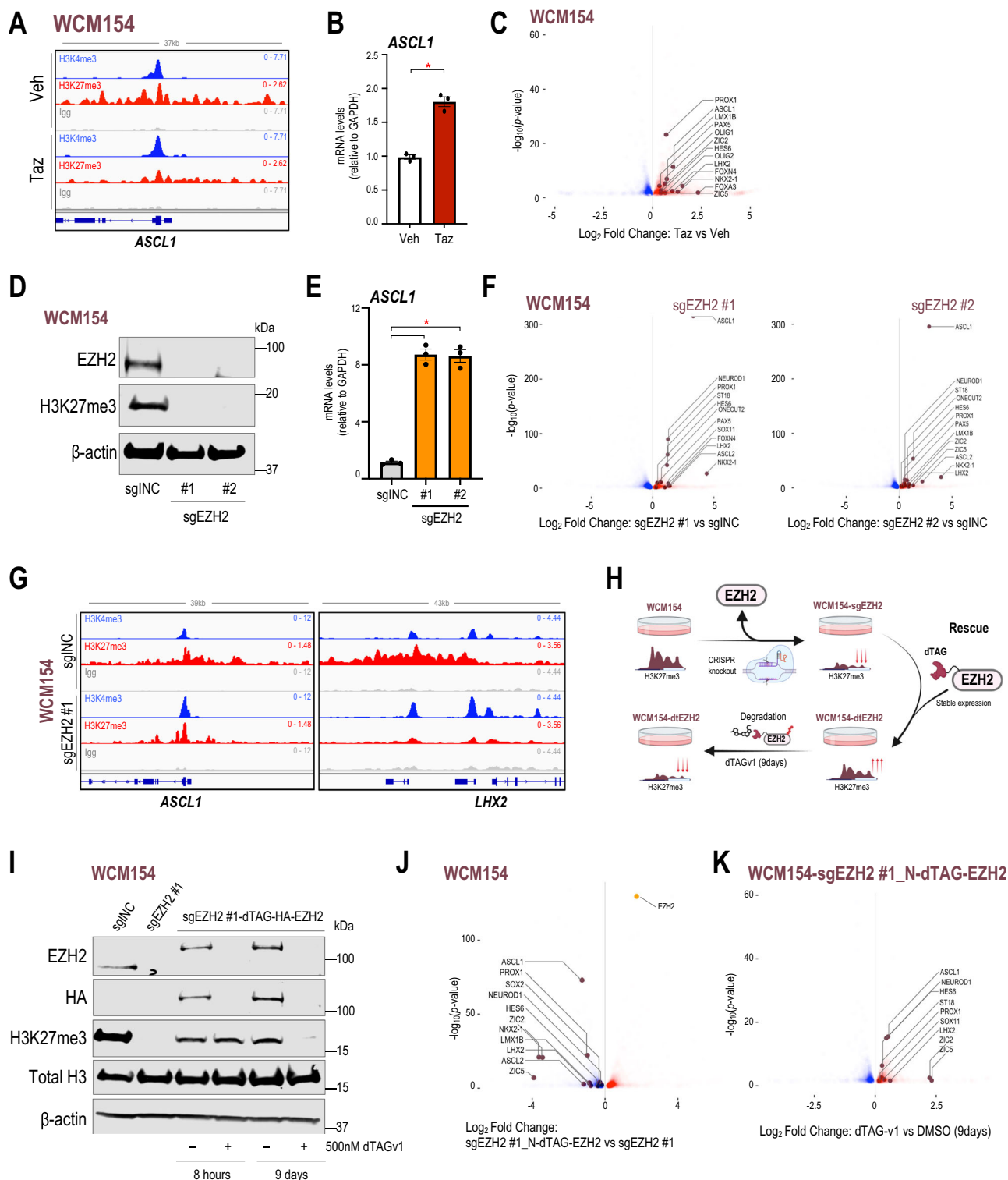
1305013903, respectively). Adhering to the protocol and institutional guidelines, written consent from the patients have been obtained for the use of their samples. Clinical and information and pathology were collected by medical record review. Tumors histology was classified as castration resistant PRAD or NEPC by a board certified pathologist. Upon pathological confirmation of a phenotype, punches were made in frozen OCT section and processed for CUT&Tag sequencing at the Centre for Functional Cancer Epigenetics at DFCI. Sequenced reads were mapped to hg38 using bowtie2 version 2.2.5

and visualized in the figures using IGV, ChIPSeeker package in R, and deepTools[62]. Broad peak calling was conducted employing MACS2[63], with a q-value (FDR) < 0.01 set as the threshold for each CUT&Tag dataset. A union set of peaks was generated using BEDTools[64]. The read counts mapped to each peak in each sample were computed from BAM files using chromVAR[65]. Subsequently, read counts for each peak were normalized through variance stabilizing transformation from DESeq2[66]. PCA and UMAP for Supplementary Fig. 2 were generated using R.

Fig. 4 | EZH2i in NEPC models induce NE-lineage genes bearing bivalent promoters. A Screenshots from Integrative Genomics Viewer (IGV) of CUT&RUN H3K27me3 or H3K4me3 or IgG levels in WCM154 treated with vehicle or tazemetostat as described in Fig. 1A at the genomic loci of *ASCL1* with vehicle or tazemetostat treatment; *gray*, IgG; *red*, H3K27me3; *blue*, H3K4me3. **B** WCM154 was treated as mentioned in Fig. 1A and samples were processed for qRT-PCR. Target gene (*ASCL1*) mRNA levels were normalized to *GAPDH* expression and are represented as relative expression using one of the values obtained from vehicle-treated conditions as 1. *Columns*, means of values (*n* = 3); *white*, vehicle; *red*, tazemetostat; *bars*, SEM values; **p*-value < 0.05, all statistical analyses used Wilcoxon two-sided tests. **C** Volcano plot of differentially expressed genes in WCM154 RNA-Seq data as described in Fig. 3A (*n* = 3/condition); *blue*, significantly downregulated genes upon tazemetostat treatment (log$_2$FoldChange < 0; *p*-value < 0.05); *red*, significantly upregulated genes upon tazemetostat treatment (log$_2$FoldChange < 0; *p*-value < 0.05); *burgundy*, NE-lineage transcription factors upregulated upon tazemetostat treatment. **D** Western blot analysis for indicated proteins showing efficiency of knockout of EZH2 in WCM154 using two independent sgRNAs targeting EZH2. Blots were reprobed for β-actin as loading control. Representative western blot from three independent experiments is shown. **E** WCM154 control or EZH2 knockout lines were processed for qRT-PCR. Target gene (*ASCL1*) mRNA levels were normalized to *GAPDH* expression and are represented as a relative expression using one of the values obtained from WCM154-sgINC conditions as 1. *Columns*, means of values (*n* = 3); *white*, WCM154-sgINC; *orange*, WCM154-sgEZH2 (#1 and #2); *bars*, SEM values; **p*-value < 0.05, all statistical analyses used Wilcoxon two-sided tests. **F** Volcano plot of differentially expressed genes in WCM154 RNA-Seq data as described in (**D**; *n* = 3/condition); *blue*, significantly downregulated genes upon EZH2 knockout treatment (log$_2$FoldChange < 0; *p*-value < 0.05); *red*, significantly upregulated genes upon EZH2 knockout treatment (log$_2$FoldChange < 0; *p*-value < 0.05); *burgundy*, NE-lineage transcription factors upregulated upon EZH2 knockout. **G** Screenshots from Integrative Genomics Viewer (IGV) of CUT&RUN H3K27me3 or H3K4me3 or IgG levels in WCM154-sgINC or sgEZH2 #1 as described in (**D**) at the genomic loci of *ASCL1* or *LHX2*; *gray*, IgG; *red*, H3K27me3; *blue*, H3K4me3. **H** Schematic of the WCM154 knockout of endogenous EZH2 and rescue using a recombinant dTAG-fused EZH2 and treatment with degrader compound (dTAGv-1) for 9 days. H3K27me3 levels are lost after EZH2 knockout and rescued (partially) after re-introduction of recombinant dTAG-EZH2 and again lowered upon 9 days of dTAGv-1 mediated degradation of EZH2. Figure 4/panel **H** Created with BioRender.com released under a Creative Commons Attribution-NonCommercial-NoDerivs 4.0 International license. **I** Western blot analysis for indicated proteins showing the efficiency of knockout of EZH2 and rescue using recombinant dTAG-EZH2 in WCM154. Impact of dTAGv-1 treatment at 8 h and 9 days is shown on levels of EZH2 and H3K27me3. Blots were reprobed for β-actin as loading control. Representative western blot from two independent experiments is shown. **J** WCM154 models with knockout of EZH2 (sgEZH2 #1) and rescue using recombinant dTAG-EZH2 were processed for RNA-Seq (*n* = 3/condition). Volcano plot of differentially expressed genes; *blue*, significantly downregulated genes upon EZH2 knockout treatment (log$_2$FoldChange < 0; *p*-value < 0.05); *red*, significantly upregulated genes upon EZH2 knockout treatment (log$_2$FoldChange < 0; *p*-value < 0.05); *orange*, EZH2 levels shown as control; *burgundy*, NE-lineage transcription factors upregulated upon rescue of EZH2 expression. **K** WCM154 models with recombinant dTAG-EZH2 treated with vehicle or dTAGv-1 for 9 days were processed for RNA-Seq (*n* = 3/condition). Volcano plot of differentially expressed genes; *blue*, significantly downregulated genes upon dTAGv-1 treatment (log$_2$FoldChange < 0; *p*-value < 0.05); *red*, significantly upregulated genes upon dTAGv-1 treatment (log$_2$FoldChange < 0; *p*-value < 0.05); burgundy, NE-lineage transcription factors upregulated upon rescue of EZH2 expression.

Western blotting and immunohistochemistry

Cells were washed twice with ice-cold phosphate-buffered saline (PBS, Gibco) and harvested in whole-cell lysis buffer (110 mM sodium dodecyl sulfate (SDS), 100 mM dithiothreitol, 80 mM Tris-HCl (pH 6.9), 10% glycerol). Cell lysates were boiled at 95 °C for 5 min. Equal amounts of protein was estimated by Lowry protocol (RCDC Protein Assay, Bio-Rad) and were subjected to NuPAGE Novex gel electrophoresis (Life Technologies). Based on the predicted molecular weight of the protein of interest, Gel electrophoresis was performed on 4–12% or 10% Bis-Tris NuPAGE gels or 3–8% Tris-Acetate NuPAGE gels. Proteins were transferred onto nitrocellulose membranes (NuPAGE) and blocked with 5% milk or bovine serum albumin prepared in tris-buffered saline with 0.1% Tween-20. Primary antibodies against H3K27me3 (cell signaling technology; cat. no. 9733 S; 1:2000 dilution) or total-histone-H3 (cell signaling technology; cat. no. 3638 S; 1:5000 dilution) or β-actin (cell signaling technology; cat. no. 8457 S or 3700 S; 1:5000 dilution) or EZH2 (cell signaling technology; cat. no. 5246 S; 1:1000 dilution), or HA-Tag (cell signaling technology; cat. no. 8457 S or 3700 S; 1:2000 dilution) or MHC Class I (OriGene; cat. no. AM33035PU-N; 1:1000 dilution) or ASCL1 (abcam; cat. no. ab211327; 1:1000 dilution) or HES6 (abcam; cat. no. ab172800; 1:1000 dilution) or CCNA2 (abcam; cat. no. ab181591; 1:1000 dilution) or CCNB1 (cell signaling technology; cat. no. 12231; 1:1000 dilution) or CCNB2 (abcam; cat. no. ab185622; 1:1000 dilution) were used as indicated in the figures. Near Infra-Red Fluorescent detection was performed using LI-COR secondary antibodies matching the host species of the primary antibodies. LI-COR Odyssey M and imaging software were used to visualize the western blots. Blots were stripped with stripping buffer (Restore Plus Western blot, ThermoFisher Scientific) and reprobed with additional primary antibodies as required.

Immunohistochemistry was performed as described previously[14].

Cell viability assays

Cell viability was measured at indicated time points after treatment using CellTiter-Glo assay (Promega) in 96-well plate format as per the manufacturer's protocol.

Flow cytometry analysis

After live/dead staining with Zombie NIR Fixable Viability Kit (cat. 423106; Biolegend) per the manufacturer's instructions, single-cell suspensions were stained with fluorophore-conjugated primary antibodies (HLA-ABC-BV510, clone W6/30, cat. 311436; Biolegend; 1:100 dilution) in PBS containing 2% v/v FBS. After washing, cells were resuspended in PBS containing 2% FBS and analyzed on a LSRFortessa flow cytometer (Becton Dickinson). Expression levels were compared with isotype control antibody (mouse IgG2a κ-BV510 Isotype Ctrl, clone MOPC-173; cat. 400268; Biolegend; 1:100 dilution). Data analyses were performed using FlowJo software (TreeStar).

Generation of cells with stable over-expression

For EZH2 CRISPR knockout: One million cells were resuspended in 20 µl of electroporation buffer (P3 solution, Lonza) and mixed ribonuclear protein complexes (RNP) of Cas9 protein with bound gRNAs. Assembly of RNPs was performed with 100 µM of tracrRNA (IDT) with 100 µM crRNAs (sgCtrl: AAA AAT GCC AAA AGT TAC CC, sgEZH2 #1: TGC GAC TGA GAC AGC TCA AG, sgEZH2 #2: TAT GAT GGG AAA GTA CAC G) at 1:1 ratio, incubated at 95 °C for 5 min followed by cooling to room temperature followed by addition of 20 µM Cas9 protein incubated for 15 mins at 37 °C. The mixtures were transferred to a 16-well Nucleocuvette Strip and nucleofection was performed in a 4D-Nucleofector (Lonza). Following nucleofection, cells were grown in 6-well plate coated with 1% collagen (ThermoFisher). Single cell selection was performed and colonies were selected based on knockout of EZH2 in western blot analysis.

For rescue of EZH2: Vector containing EZH2 cDNA was purchased from Addgene (#81742) and site directed mutagenesis (Agilent) was performed to add a stop codon (Fwd 5′–3′, AGA AAG TTG GGC ATC AAG GGA TTT CCA TTT CTC TTT CGA TG; Rev 5′–3′, CAT CGA AAG AGA AAT GGA AAT CCC TTG ATG CCC AAC TTT CT) and remove the start codon (Fwd 5′–3′, TTC TTC CCA GTC TGG CCG CCA ACT TTT TTG TAC A; Rev 5′–3′, TGT ACA AAA AGT TGG CGG CCA GAC TGG GAA GAA A). Gateway cloning (NEB) LR reaction was performed using the modified construct and destination vector (Addgene #91797) to produce pLEX_305-N-dTAG-HA-EZH2. The destination vector was a
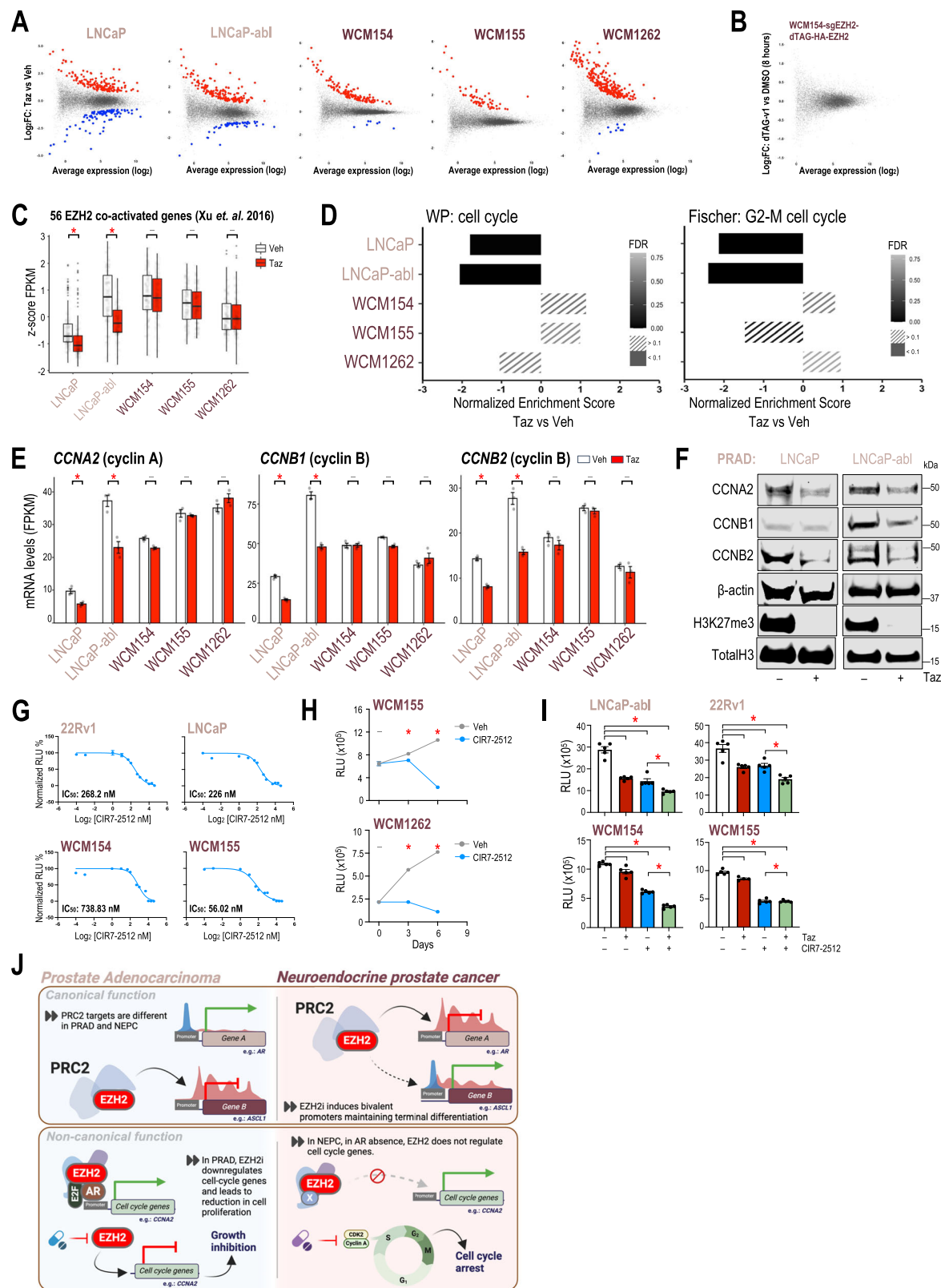
generous gift from Dr. William Kaelin lab. This plasmid was co-transfected with pMD2.G and psPAX2 using Lipofectamine 3000 (Invitrogen) into HEK293FT cells to generate viral particles. Lentiviral supernatants and 10 μg/ml Polybrene were added and incubated with cell lines mentioned in the figures. Infected cell lines were selected with antibiotics as described in the constructs. Over-expression of the desired proteins was confirmed by western blot analysis as described above.

Epigenetic and transcriptomic studies

ChIP-qPCR. ChIP was performed using 5–7 million cells in a 10 cm dish. Cells were washed with ice-cold PBS containing EDTA-free

Fig. 5 | Non-canonical activity of EZH2 is limited to PRAD models. A Scatter plot of differentially expressed genes in PRAD and NEPC models in RNA-Seq data as described in Fig. 1A ($n = 3$/condition/model); *blue*, significantly downregulated genes upon tazemetostat treatment (log$_2$FoldChange < 0.5; *p*-value < 0.05); *red*, significantly upregulated genes upon tazemetostat treatment (log$_2$FoldChange > 0.5; *p*-value < 0.05). **B** Scatter plot of differentially expressed genes in WCM154-sgEZH2 #1-dTAG-N-EZH2 rescue model in RNA-Seq data as described in Fig. 4H upon treatment with vehicle or dTAGv-1 treatment for 8 h ($n = 3$/condition; log$_2$FoldChange < 0.5; *p*-value < 0.05). **C** Box plot summary of cumulative *z*-score of FPKM values (from Fig. 3A; $n = 3$) of 56 genes co-activated by EZH2 reported in Xu et al.[20]; *white*, vehicle treatment; *red*, tazemetostat treatment; *bars*, center of box represents median, the lower and upper hinges correspond to the 25th and 75th percentiles, the upper whisker extends from the hinge to the largest value no further than 1.5 times inter-quartile range (IQR), the lower whisker extends from the hinge to the smallest value at most 1.5 times IQR of the hinge, data beyond the end of the whiskers are outliers and are plotted individually; –, *p*-value < 0.05; *, *p*-value < 0.05, all statistical analyses used Wilcoxon two-sided tests. **D** Cells or organoids of PRAD (pink) or NEPC (burgundy) models were treated as indicated in Fig. 3A ($n = 3$/condition) and RNA was isolated and processed for RNA-seq. GSEA analysis was performed and normalized enrichment score are plotted for the indicated pathway; *gray-black gradient*, FDR values. **E** FPKM values of *CCNA2, CCNB1*, and *CCNB2* from the RNA-seq (Fig. 3A; $n = 3$/condition) in vehicle or taze-metostat treated conditions in indicated models. *Columns*, means of values ($n = 3$/condition/model); *white*, vehicle treatment; *red*, tazemetostat treatment; *bars*, SEM

values; –, *p*-value < 0.05; *, *p*-value < 0.05, all statistical analyses used Wilcoxon two-sided tests. **F** Western blot analysis of LNCaP and LNCaP-abl samples treated with vehicle (DMSO) or 5 µM tazemetostat for 6 days as described in Fig. 1A ($n = 3$/condition), showing downregulation of indicated cyclins along with reduced levels of H3K27me3. Blots were reprobed for β-actin and total H3 as loading controls. Representative western blot from three independent experiments is shown. **G** IC$_{50}$ dose response curves in PRAD (pale pink) and NEPC (burgundy) using increasing dose of CIR7-2512. dots, means of values ($n = 5$); *bars*, SEM values. **H** NEPC (burgundy) models were treated with vehicle (Veh; DMSO) or 500 nM CIR7-2512 for indicated number of days and cell viability was performed. dots, means of values ($n = 5$); *grey*, vehicle treatment; *blue*, tazemetostat treatment; *bars*, SEM values; –, *p*-value < 0.05; *, *p*-value < 0.05, all statistical analyses used Wilcoxon two-sided tests. **I** Prostate cancer models (Left panel – AR-driven PRAD; right panel – AR-indifferent NEPC) were treated with vehicle (Veh; DMSO) or 5 µM of tazemetostat (Taz) or 500 nM CIR7-2512 or in combination. CellTiter-Glo® luminescent cell viability assay was performed after 6 days of treatment. *Columns*, means of values ($n = 5$; WCM155, Taz treatment; $n = 4$); *white*, vehicle treatment; *red*, tazemetostat treatment; *blue*, CIR7-2512 treatment; *green*, combination treatment; *bars*, SEM values; –, *p*-value > 0.05 (not significant); *, *p*-value < 0.05, all statistical analyses used Wilcoxon two-sided tests. **J** Schematic of the differences in canonical and non-canonical function of EZH2 in prostate adenocarcinoma compared to neuroendocrine prostate cancer. Figure 5/panel J Created with BioRender.com released under a Creative Commons Attribution-NonCommercial-NoDerivs 4.0 International license.

---

protease inhibitor (Roche) and 5 mM sodium butyrate. Crosslinking was performed using 1% methanol-free formaldehyde (invitrogen) for 5 mins, quenched by adding 0.125 M glycine for 5 mins. Cells were scraped and centrifuged to pellet down at $600 \times g$ for 2 mins. Pelleted cells were lysed using sarkosyl lysis buffer (0.1%SDS, 1x TX-100, 10 mM Tris-HCl pH = 8, 1 mM EDTA pH = 8, 0.1% Sodium Deoxycholate, 0.25% sarkosyl, 0.3 mM NaCl, EDTA-free protease inhibitor (Roche) and 5 mM Sodium butyrate). Sonication was performed using Covaris machine in 1 ml tubes (Covaris) at 5% duty factor, 140 PIP, 200 cycles per burst, for 5 mins. Chromatin immunoprecipitation was performed overnight using antibodies conjugated with dynabeads (invitrogen) against IgG control (cell signaling technology, cat. no. 3900 S, 1 µg/reaction) or H3K27me3 (cell signaling technology, cat. no. 9733 S, 1 µg/reaction) or H3K4me3 (cell signaling technology, cat. no. 9751 S, 1 µg/reaction). After 5 washes with wash buffer (HEPES-based RIPA buffer), elution buffer (1%SDS, 0.1 M NaHCO$_3$) was added to the beads. RNAse treatment was performed for an hour at 37 °C followed by 16 h of Proteinase K treatment at 65 °C overnight. DNA was purified (Qiagen) and qPCR was performed using primers mentioned in the table below along with 0.1% input.

CUT&RUN. CUT&RUN studies were performed with 100,000 cells in duplicates using a kit from Epicypher adhering to manufacturer's protocol using antibodies against IgG or H3K4me3 (Epicypher, cat. no. 13-0041, 0.5 µg per reaction) or H3K27me3 (Invitrogen, cat. no. MA511198, 0.5 µg per reaction). Automated library-preparation and sequencing were performed by Molecular Biology Core Facilities at Dana-Farber Cancer Institute. Sequencing reads were mapped to hg38 human genome reference using bwa and visualized using deepTools as plotProfiles.

Motif analysis. HOMER motif analysis was performed for genes of interest setting promoter region to 1000 bp upstream and down-stream from TSS, and default motif length of 8,10, or 12.

RNA-Seq and qRT-PCR. Total RNA isolated (QIAGEN) was submitted to Novogene for paired-end sequencing. Sequencing reads were mapped to hg38 human genome reference using STAR-RSEM. Differential gene expression analysis was performed using the limma and edgeR and GSEA software was used to perform pathway analysis. Gene ontology analysis was performed using hypergeometric overlap

statistic tool to calculate the overlap between a gene list and pathways in Molecular signature database. Bar graphs and heatmaps were generated using sample FPKM values.

qRT-PCR. RNA was isolated ($n = 3$) (QIAGEN) and complementary DNA (cDNA) was prepared from 500 ng total RNA (Bio-Rad). Quantitative Real-time reverse transcription–PCR (qRT–PCR) was done using SYBR Green PCR mastermix (Bio-Rad) on a Bio-Rad qPCR system. Primers sequences are mentioned in the table below. Relative quantification was calculated using the ΔCt method normalized to GAPDH levels.

Target	Assay	Forward primer (5' to 3')	Reverse primer (5' to 3')
GAPDH	qRT-PCR	GAAGGTGAAGGTCGGAGTC	GAAGATGGTGATGGGATTTC
ASCL1	qRT-PCR	GAAGATGGTGATGGGATTTC	CAAAGCCCAGGTTGACCA
SYPL2	qRT-PCR	GCTGGGCTTCATCAAAGTTC	GAAGGGATAGCCAAATGCAA
TMEFF2	qRT-PCR	CTGCATGCAAACAGCAGAGT	CTGCACCAAACTGGCAAATA
SYPL2	ChIP-qPCR	CTTAGTGGCAGGAGGGTGAA	ACCAAGGAGTGGTATGTGCAG
TMEFF2	ChIP-qPCR	GGCGTTTGGCAGTCACTTA	GTCATGGTGCTGTGGGAGT

Animal studies

All animal studies were approved by the Dana-Farber Cancer Institute (DFCI) or Weill Cornell Medicine Institutional Animal Care and Use Committee (IACUC). Mice were housed in solid-bottom, polysulfone 75 sq. in. microisolator cages. The cages are used in conjunction with integrated automatic watering. Temperature and humidity were controlled at 72 +/– 2 °F and a target range of 35–55% relative humidity. A standard photoperiod of 12 h light/12 h dark were controlled by an automated system. Maximum permitted tumor volume is 2 cm^3 and was not exceeded in any of our studies.

WCM12 PDX tumors were subcutaneously implanted were injected to right flank of 6–8 weeks-old NSG male mice (NOD.Cg-Prkdc^{scid}Il2rg^{tm1Wjl}/SzJ, the Jackson laboratory). Tumor volumes defined as 0.5 × length × width^2 and the body weights were measured every two days. Mice were randomly assigned into vehicle or tazemetostat group once their tumors reach 100 mm^3. Mice were treated with vehicle (0.5% Methylcellulose (400 cps), 0.1% Tween80, pH4.0) or tazemetostat (250 mg/kg) b.i.d. p.o. for indicated number of days. The mice were euthanized in a CO$_2$ chamber adhering IACUC guidelines. At necropsy, tumor size, tumor weight, and body weight were measured to evaluate the drug effect and toxicity.

MSKPCa4 organoids, kindly shared by Dr. Yu Chen from Memorial Sloan Kettering Cancer Center, were dissociated into single cells and 4 million cells were mixed 50:50 with Matrigel and injected into CB17 SCID mice for subcutaneous growth. Once the tumors were obtained, they were subsequently passaged in vivo for the experiment. GSK126 (150 mg/kg) or vehicle was administered q.d. i.p. at a dose volume in 20% captisol adjusted to pH 4–4.5 with 1 N acetic acid.

Statistical analysis

Standard two-tailed Student t-tests and nonparametric tests were performed to analyze statistical significance of two groups. Two-way ANOVA tests were performed to examine the statistical significance of datasets with grouped analyses. Statistical significance was set at $p < 0.05$ in this study. All graphs and statistical analyses were completed using GraphPad Prism or ggplot package in R or deepTools. Pearson correlation was used for nearest neighbor analysis and pairwise-correlation. No statistical method was used to predetermine sample size. Except for animal studies, experiments were not randomized, and investigators were not blinded to allocation during experiments and outcome assessment.

Reporting summary

Further information on research design is available in the Nature Portfolio Reporting Summary linked to this article.

Data availability

The raw sequencing and processed data (RNA-Seq, CUT&RUN, and CUT&Tag) data generated in this study have been deposited in the public repository (Gene Expression Omnibus) under accession codes GSE256220 and GSE256194. Source data are provided with this paper as a Source Data file. The Baca et al. publicly available data used in this study are available in the public repository (Gene Expression Omnibus) under accession code GSE161948[31]. Source data are provided with this paper.

References

1. Quintanal-Villalonga, A. et al. Lineage plasticity in cancer: a shared pathway of therapeutic resistance. *Nat. Rev. Clin. Oncol.* **17**, 360–371 (2020).
2. Beltran, H. et al. The role of lineage plasticity in prostate cancer therapy resistance. *Clin. Cancer Res.* **25**, 6916–6924 (2019).
3. Aggarwal, R. et al. Clinical and genomic characterization of treatment-emergent small-cell neuroendocrine prostate cancer: a multi-institutional prospective study. *J. Clin. Oncol.* **36**, 2492–2503 (2018).
4. Abida W. et al. Genomic correlates of clinical outcome in advanced prostate cancer. *Proc. Natl Acad. Sci. USA.* https://doi.org/10.1073/pnas.1902651116, https://www.ncbi.nlm.nih.gov/pubmed/31061129 (2019).
5. Beltran, H. et al. Molecular characterization of neuroendocrine prostate cancer and identification of new drug targets. *Cancer Discov.* **1**, 487–495 (2011).
6. Feinberg, A. P. & Levchenko, A. Epigenetics as a mediator of plasticity in cancer. *Science* **379**, eaaw3835 (2023).
7. Hanahan, D. Hallmarks of cancer: new dimensions. *Cancer Discov.* **12**, 31–46 (2022).
8. Beltran, H. et al. Divergent clonal evolution of castration-resistant neuroendocrine prostate cancer. *Nat. Med.* **22**, 298–305 (2016).
9. Tang, F. et al. Chromatin profiles classify castration-resistant prostate cancers suggesting therapeutic targets. *Science* **376**, eabe1505 (2022).
10. Zhao, S. G. et al. The DNA methylation landscape of advanced prostate cancer. *Nat. Genet.* **52**, 778–789 (2020).
11. Cejas, P. et al. Subtype heterogeneity and epigenetic convergence in neuroendocrine prostate cancer. *Nat. Commun.* **12**, 5775 (2021).
12. Davies, A., Zoubeidi, A., Beltran, H. & Selth, L. A. The transcriptional and epigenetic landscape of cancer cell lineage plasticity. *Cancer Discov.* **13**, 1771–1788 (2023).
13. Margueron, R. & Reinberg, D. The Polycomb complex PRC2 and its mark in life. *Nature* **469**, 343–349 (2011).
14. Puca, L. et al. Patient derived organoids to model rare prostate cancer phenotypes. *Nat. Commun.* **9**, 2404 (2018).
15. Bracken, A. P., Dietrich, N., Pasini, D., Hansen, K. H. & Helin, K. Genome-wide mapping of polycomb target genes unravels their roles in cell fate transitions. *Genes Dev.* **20**, 1123–1136 (2006).
16. Schuettengruber, B. & Cavalli, G. Recruitment of polycomb group complexes and their role in the dynamic regulation of cell fate choice. *Development* **136**, 3531–3542 (2009).
17. Bernstein, B. E. et al. A bivalent chromatin structure marks key developmental genes in embryonic stem cells. *Cell* **125**, 315–326 (2006).
18. Jadhav, U. et al. Acquired tissue-specific promoter bivalency is a basis for PRC2 necessity in adult cells. *Cell* **165**, 1389–1400 (2016).
19. Xu, K. et al. EZH2 oncogenic activity in castration-resistant prostate cancer cells is polycomb-independent. *Science* **338**, 1465–1469 (2012).
20. Xu, H. et al. Integrative analysis reveals the transcriptional collaboration between EZH2 and E2F1 in the regulation of cancer-related gene expression. *Mol. Cancer Res.* **14**, 163–172 (2016).
21. Wang, J. et al. EZH2 noncanonically binds cMyc and p300 through a cryptic transactivation domain to mediate gene activation and promote oncogenesis. *Nat. Cell Biol.* **24**, 384–399 (2022).
22. Morel, K. L. et al. EZH2 inhibition activates a dsRNA-STING-interferon stress axis that potentiates response to PD-1 checkpoint blockade in prostate cancer. *Nat. Cancer* **2**, 444–456 (2021).
23. Liao Y. et al. Inhibition of EZH2 transactivation function sensitizes solid tumors to genotoxic stress. *Proc Natl Acad Sci USA.* 2022;119. https://doi.org/10.1073/pnas.2105898119, https://www.ncbi.nlm.nih.gov/pubmed/35031563.
24. Jadhav, U. et al. Replicational dilution of H3K27me3 in mammalian cells and the role of poised promoters. *Mol. Cell* **78**, 141–51.e5 (2020).
25. Keam, S. J. Valemetostat tosilate: first approval. *Drugs* **82**, 1621–1627 (2022).
26. Yamazaki, S., Gukasyan, H. J., Wang, H., Uryu, S. & Sharma, S. Translational pharmacokinetic-pharmacodynamic modeling for an orally available novel inhibitor of epigenetic regulator enhancer of Zeste Homolog 2. *J. Pharm. Exp. Ther.* **373**, 220–229 (2020).
27. McCabe, M. T. et al. EZH2 inhibition as a therapeutic strategy for lymphoma with EZH2-activating mutations. *Nature* **492**, 108–112 (2012).
28. Ku, S. Y. et al. Rb1 and Trp53 cooperate to suppress prostate cancer lineage plasticity, metastasis, and antiandrogen resistance. *Science* **355**, 78–83 (2017).
29. Davies, A. et al. An androgen receptor switch underlies lineage infidelity in treatment-resistant prostate cancer. *Nat. Cell Biol.* **23**, 1023–1034 (2021).
30. Juan, A. H. et al. Roles of H3K27me2 and H3K27me3 examined during fate specification of embryonic stem cells. *Cell Rep.* **17**, 1369–1382 (2016).
31. Baca, S. C. et al. Reprogramming of the FOXA1 cistrome in treatment-emergent neuroendocrine prostate cancer. *Nat. Commun.* **12**, 1979 (2021).
32. Burr, M. L. et al. An evolutionarily conserved function of polycomb silences the MHC class I antigen presentation pathway and enables immune evasion in cancer. *Cancer Cell* **36**, 385–401.e8 (2019).
33. Xiao, L. et al. Epigenetic reprogramming with antisense oligonucleotides enhances the effectiveness of androgen receptor

inhibition in castration-resistant prostate cancer. *Cancer Res.* **78**, 5731–5740 (2018).

34. Puca L. et al. Delta-like protein 3 expression and therapeutic targeting in neuroendocrine prostate cancer. *Sci. Transl. Med.* 2019;11. https://doi.org/10.1126/scitranslmed.aav0891, https://www.ncbi.nlm.nih.gov/pubmed/30894499.

35. Namekawa, T. et al. NPTX1 is a novel serum biomarker induced by ARPI treated prostate cancer and enriched in lineage plasticity with BRN2 high. *J. Urol.* **209**, e277 (2023).

36. Nabet, B. et al. Rapid and direct control of target protein levels with VHL-recruiting dTAG molecules. *Nat. Commun.* **11**, 4687 (2020).

37. Stengel, K. R., Ellis, J. D., Spielman, C. L., Bomber, M. L. & Hiebert, S. W. Definition of a small core transcriptional circuit regulated by AML1-ETO. *Mol. Cell* **81**, 530–45.e5 (2021).

38. Muhar, M. et al. SLAM-seq defines direct gene-regulatory functions of the BRD4-MYC axis. *Science* **360**, 800–805 (2018).

39. Layden, H. M., Eleuteri, N. A., Hiebert, S. W. & Stengel, K. R. A protocol for rapid degradation of endogenous transcription factors in mammalian cells and identification of direct regulatory targets. *STAR Protoc.* **2**, 100530 (2021).

40. Chen, Y. N. et al. Selective killing of transformed cells by cyclin/cyclin-dependent kinase 2 antagonists. *Proc. Natl Acad. Sci. USA* **96**, 4325–4329 (1999).

41. Garcia, P. D. et al. Macrocycles inhibiting RxL-mediated binding of substrates to Cyclin A are synthetic lethal in Rb mutated small cell lung carcinoma (SCLC). *Cancer Res.* **82**, 5379 (2022).

42. Hoffman R. The discovery of PF-07104091: A CDK2 selective inhibitor for the treatment of cyclinE amplified cancers. *AACR Annual Meeting* (2021).

43. Arora, M. et al. Rapid adaptation to CDK2 inhibition exposes intrinsic cell-cycle plasticity. *Cell* **186**, 2628–43.e21 (2023).

44. Ianevski, A., Giri, A. K. & Aittokallio, T. SynergyFinder 3.0: an interactive analysis and consensus interpretation of multi-drug synergies across multiple samples. *Nucleic Acids Res.* **50**, W739–W743 (2022).

45. Mu, P. et al. SOX2 promotes lineage plasticity and antiandrogen resistance in TP53- and RB1-deficient prostate cancer. *Science* **355**, 84–88 (2017).

46. Macrae, T. A., Fothergill-Robinson, J. & Ramalho-Santos, M. Regulation, functions and transmission of bivalent chromatin during mammalian development. *Nat. Rev. Mol. Cell Biol.* **24**, 6–26 (2023).

47. Brown, R., Curry, E., Magnani, L., Wilhelm-Benartzi, C. S. & Borley, J. Poised epigenetic states and acquired drug resistance in cancer. *Nat. Rev. Cancer* **14**, 747–753 (2014).

48. Bernards, R., Dessain, S. K. & Weinberg, R. A. N-myc amplification causes down-modulation of MHC class I antigen expression in neuroblastoma. *Cell* **47**, 667–674 (1986).

49. Gartin, A. K. et al. Merkel cell carcinoma sensitivity to EZH2 inhibition is mediated by SIX1 derepression. *J. Invest. Dermatol.* **142**, 2783–92.e15 (2022).

50. Paulson, K. G. et al. Acquired cancer resistance to combination immunotherapy from transcriptional loss of class I HLA. *Nat. Commun.* **9**, 3868 (2018).

51. Mahadevan, N. R. et al. Intrinsic immunogenicity of small cell lung carcinoma revealed by its cellular plasticity. *Cancer Discov.* **11**, 1952–1969 (2021).

52. Leon, T. E. et al. EZH2-Deficient T-cell acute lymphoblastic leukemia is sensitized to CHK1 inhibition through enhanced replication stress. *Cancer Discov.* **10**, 998–1017 (2020).

53. Kim, K. H. & Roberts, C. W. Targeting EZH2 in cancer. *Nat. Med* **22**, 128–134 (2016).

54. Bracken, A. P. et al. EZH2 is downstream of the pRB-E2F pathway, essential for proliferation and amplified in cancer. *EMBO J.* **22**, 5323–5335 (2003).

55. Kazansky Y. et al. Overcoming clinical resistance to EZH2 inhibition using rational epigenetic combination therapy. *Cancer Discov.* https://doi.org/10.1158/2159-8290.CD-23-0110, https://www.ncbi.nlm.nih.gov/pubmed/38315003 (2024).

56. Drosos, Y. et al. NSD1 mediates antagonism between SWI/SNF and polycomb complexes and is required for transcriptional activation upon EZH2 inhibition. *Mol. Cell* **82**, 2472–89.e8 (2022).

57. Venkadakrishnan, V. B., Yamada, Y., Weng, K., Idahor, O. & Beltran, H. Significance of RB loss in unlocking phenotypic plasticity in advanced cancers. *Mol. Cancer Res.* **21**, 497–510 (2023).

58. Hsu, J. H. et al. EED-targeted PROTACs degrade EED, EZH2, and SUZ12 in the PRC2 complex. *Cell Chem. Biol.* **27**, 41–6.e17 (2020).

59. Velez, J. et al. Discovery of a novel, highly potent EZH2 PROTAC degrader for targeting non-canonical oncogenic functions of EZH2. *Eur. J. Med Chem.* **267**, 116154 (2024).

60. Franceschini G. M. et al. Non-invasive detection of neuroendocrine prostate cancer through targeted cell-free DNA methylation. *Cancer Discov.* https://doi.org/10.1158/2159-8290.CD-23-0754, https://www.ncbi.nlm.nih.gov/pubmed/38197680 (2024).

61. Culig, Z. et al. Switch from antagonist to agonist of the androgen receptor bicalutamide is associated with prostate tumour progression in a new model system. *Br. J. Cancer* **81**, 242–251 (1999).

62. Langmead, B. & Salzberg, S. L. Fast gapped-read alignment with Bowtie 2. *Nat. Methods* **9**, 357–359 (2012).

63. Zhang, Y. et al. Model-based analysis of ChIP-Seq (MACS). *Genome Biol.* **9**, R137 (2008).

64. Quinlan, A. R. & Hall, I. M. BEDTools: a flexible suite of utilities for comparing genomic features. *Bioinformatics* **26**, 841–842 (2010).

65. Schep, A. N., Wu, B., Buenrostro, J. D. & Greenleaf, W. J. chromVAR: inferring transcription-factor-associated accessibility from single-cell epigenomic data. *Nat. Methods* **14**, 975–978 (2017).

66. Love, M. I., Huber, W. & Anders, S. Moderated estimation of fold change and dispersion for RNA-seq data with DESeq2. *Genome Biol.* **15**, 550 (2014).

Acknowledgements

Author contributions

Conceptualization: V.B.V., H.B. Methodology: V.B.V., M.A.B., N.R.M., K.M., L.P., Z.T.H. Software: V.B.V., M.A.B., A.A.B., Z.T.H., M.Y.T. Validation: V.B.V., A.G.P., K.W., N.C.E.V., O.I. Formal Analysis: V.B.V., M.A.B., K.W., N.C.E.V., N.R.M., K.M., L.P., O.I., A.A.B. Investigation: V.B.V., A.G.P., M.A.B., N.A.T., K.W., N.C.E.V., N.R.M., K.M., L.P., O.I. Resources: V.B.V., N.R.M., Z.T.H., M.Y.T., D.A.B., M.B., H.B. Data Curation: V.B.V., M.A.B. Writing – Original Draft: V.B.V., H.B. Writing – Review & Editing: V.B.V., A.G.P., R.S., M.A.B., N.A.T., K.W., N.C.E.V., N.R.M., K.M., L.P., O.I., S.Y.K., M.K.B., A.A.B., Z.T.H., M.Y.T., D.A.B., D.S.R, M.B., H.B. Visualization: V.B.V., A.G.P., M.A.B., K.W., N.R.M., K.M. Supervision: V.B.V., Z.T.H., M.Y.T., D.A.B., D.S.R., M.B., H.B. Project administration: V.B.V., H.B. Funding acquisition: V.B.V., H.B.

Competing interests

Additional information